DISCOVERY OF SPATIAL AND SPECTRAL STRUCTURE IN THE X-RAY EMISSION FROM THE CRAB NEBULA

MARTIN C. WEISSKOPF,[1] J. JEFF HESTER,[2] ALLYN F. TENNANT,[1] RONALD F. ELSNER,[1] NORBERT S. SCHULZ,[3]
HERMAN L. MARSHALL,[3] MARGARITA KAROVSKA,[4] JOY S. NICHOLS,[4] DOUGLAS A. SWARTZ,[5]
JEFFERY J. KOLODZIEJCZAK,[1] AND STEPHEN L. O'DELL[1]

ABSTRACT

The *Chandra X-Ray Observatory* observed the Crab Nebula and pulsar during orbital calibration. Zeroth-order images with the High-Energy Transmission Grating (HETG) readout by the Advanced CCD Imaging Spectrometer spectroscopy array (ACIS-S) show a striking richness of X-ray structure at a resolution comparable to that of the best ground-based visible-light observations. The HETG–ACIS-S images reveal, for the first time, an X-ray inner ring within the X-ray torus, the suggestion of a hollow-tube structure for the torus, and X-ray knots along the inner ring and (perhaps) along the inward extension of the X-ray jet. Although complicated by instrumental effects and the brightness of the Crab Nebula, the spectrometric analysis shows systematic variations of the X-ray spectrum throughout the nebula.

Subject headings: ISM: individual (Crab Nebula) — pulsars: individual (Crab Pulsar) —
radiation mechanisms: nonthermal — stars: neutron — supernova remnants — X-rays: general

1. INTRODUCTION

The Crab Nebula is the archetypal filled-center supernova remnant, or *plerion* (Weiler & Panagia 1978). Unlike shell-like supernova remnants, a central pulsar presumably powers each filled-center supernova remnant. Thus, the inner nebula of a plerion is particularly interesting, since it is the site of conversion of pulsar-supplied energy into synchrotron-emitting electrons. Although this general picture seems valid, details of the coupling mechanism (e.g., Rees & Gunn 1974; Dobrowolny & Ferrari 1976; Kennel & Coroniti 1984; Michel 1985; Emmering & Chevalier 1987; Coroniti 1990; Begelman & Li 1992; Michel 1994) remain uncertain.

Detailed studies (Hester et al. 1995) with the *Hubble Space Telescope* (*HST*) illustrate the rich structure of the Crab Nebula's synchrotron emission, on scales down to 0″.2. Especially intriguing are the structures of the inner nebula near the pulsar—wisps (Scargle 1969), knots, and fibrous texture (Hester et al. 1995)—which exhibit cylindrical symmetry. *HST* observations (Hester 1998) also show that wisps form and dissipate over a few weeks while moving outward at about $0.5c$, thus clarifying the dynamical nature of these features (Scargle 1969).

Even more dramatic are the X-ray images, which clearly show this cylindrical morphology. In a remarkable synthesis from lunar-occultation, modulation-collimator, and low-resolution–imaging X-ray observations, Aschenbach & Brinkmann (1975) had interpreted the extant data in terms of an X-ray torus. Subsequent, higher resolution X-ray data—from *Einstein* (Brinkmann, Aschenbach, & Langmeier 1985), *ROSAT* (Hester et al. 1995; Greiveldinger & Aschenbach 1999), and *Chandra* (reported here)—confirm this morphology

and detect a jet and counterjet nearly along the axis of the torus.

On 1999 July 23, NASA's shuttle Columbia launched the *Chandra X-Ray Observatory*. The half-power diameter of the *Chandra* system-level point-spread function is about 0″.8, at least a factor of 5 better than that of any other X-ray observatory and comparable to that of the best visible-light ground observations. Thus, *Chandra* provides an excellent tool for probing the rich structure of the inner Crab Nebula in X-rays. Here, we report the first high-spatial-resolution observation (§ 2) and describe the observed morphology (§ 3) and spectrum (§ 4) of the Crab Nebula, as obtained with *Chandra*.

2. OBSERVATION AND ANALYSIS

On 1999 August 29, during orbital calibration, *Chandra* obtained a 2667 s observation of the Crab Nebula using the High-Energy Transmission Grating (HETG; C. R. Canizares et al. 2000, in preparation) and the Advanced CCD Imaging Spectrometer spectroscopy array (ACIS-S; G. P. Garmire et al. 2000, in preparation) of six CCDs. The data include events in both zero and higher spectral order, the latter being dispersed along two crossed tracks, owing to the slightly different orientation of the High-Energy Grating facets from the Medium-Energy Grating facets. Here, we examine only the zeroth-order image of the Crab Nebula.

Figure 1 shows the HETG–ACIS-S image of the Crab Nebula for the centermost ACIS-S CCD—designated "S3"—which is one of two back-illuminated CCDs in the 10-CCD ACIS focal plane. The *Chandra* X-Ray Center's standard processing has applied aspect corrections and compensated for dither (which averages pixel-to-pixel variations of the detector) over a $16'' \times 16''$ area. Acquired in the timed-exposure graded mode at 3.241 s frame^{-1}, the data comprise an event list, with each event recorded in a 3×3 pixel "island" in which each ACIS pixel is about 0″.5 (actually, 0″.492) square. In this mode, the on-board software detects events and grades them according to which pixels (including the central pixel) have enough charge to exceed predefined thresholds.

Owing to the X-ray brilliance of the Crab Nebula and pulsar, *Chandra* observations of this source are particularly challeng-

[1] Space Science Department, NASA Marshall Space Flight Center, SD50, Huntsville, AL 35812.
[2] Department of Physics and Astronomy, Arizona State University, Tyler Mall, Tempe, AZ 85287.
[3] Center for Space Research, Massachusetts Institute of Technology, Cambridge, MA 02139.
[4] Harvard-Smithsonian Center for Astrophysics, 60 Garden Street, Cambridge, MA 02138.
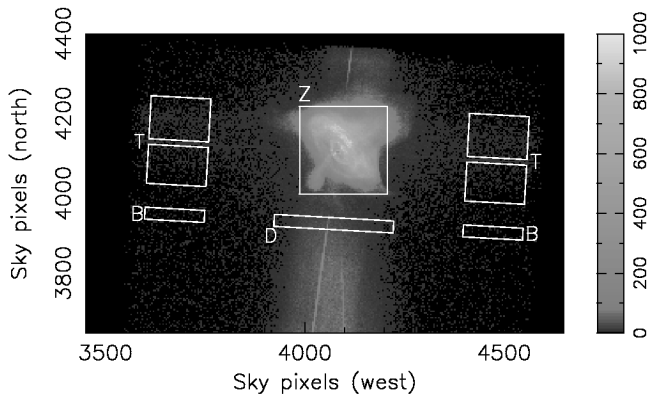[5] Universities Space Research Association, NASA Marshall Space Flight Center, SD50, Huntsville, AL 35812.

Fig. 1.—*Chandra* HETG–ACIS-S image of the Crab Nebula on CCD S3. Each sky pixel is about $0''.5$ (actually, $0''.492$). The nearly vertical, narrow X is the pulsar's dispersed spectrum; the nearly horizontal line is its trailed image. Boxes labeled T denote regions used for analyzing the trailed image of the nebula (§ 4); boxes labeled B, for determining halo surface brightness; and box D, for establishing the first-order trailed image in boxes labeled B. Box Z encloses the region examined for spectral-hardness variations (§ 4) in the timed-exposure image. The gray-scale bar indicates counts per 4×4 pixel spatial bin.

Fig. 2.—Zoomed *Chandra* HETG–ACIS-S image of the central $200'' \times 200''$ of the Crab Nebula. Previously undiscovered X-ray features include the inner ring and its knots, apparent lateral striations and circular structures at the toroid's extremities, and inward extension of the jet and counterjet. The color bar indicates counts per pixel.

ing. First, the total count rate is so high that the ACIS data saturates telemetry, resulting in dropped ACIS frames. Although this results in lost events, it does so in an unbiased manner and is not a substantive problem.

More problematic is "pileup," in which multiple photons contribute charge to the same or adjacent pixels, thus appearing as a single detected event. First, pileup effects "grade migration," changing the grade of a valid event to a grade that might normally be excluded. To mitigate this, we retained all telemetered grades in the imaging analysis (§ 3), but not in the spectral analysis (§ 4). Second, in regions of high surface brightness, the detected event rate is not proportional to the photon rate, thus reducing contrast. In regions of very high surface brightness, the pileup is so extreme that the charge deposited in a 3×3 pixel island exceeds a predetermined threshold (corresponding to about 15 keV), causing on-board rejection of the event. This "saturation" results in no detected events in the very brightest areas of the image—namely, at the position of the pulsar (Figs. 1 and 2).

To assess the impact of pileup on the spectral distribution, we analyzed the "trailed" image (Fig. 1). The trailed image results from X-rays that strike the CCD while the frame-transfer electronics are moving the exposed frame into the CCD's frame-store region. As each of the 1024 rows transfers toward the frame-store region, it spends about 40 μs at each physical row. Compared to the 3.20 s integration time per frame, the 41 ms frame-transfer time is quite small, so pileup is negligible for the trailed image. Of course, the trailed image has no spatial information in the transfer (trail) direction.

The region from which we extracted the trailed image also contains photons from the timed exposure of the Crab Nebula's X-ray halo. To subtract this component from the trailed image, we obtained a "background" from regions labeled B (Fig. 1). A further complication is the presence in region B of a component due to the trailed image of the first-order dispersed spectrum of the Crab Nebula. Because this contribution is small, we simply scaled the flux in region D of the dispersed image by $300(4 \times 10^{-5})/3.20 = 0.0038$—the number of rows occupied by the first-order image of the Crab Nebula times
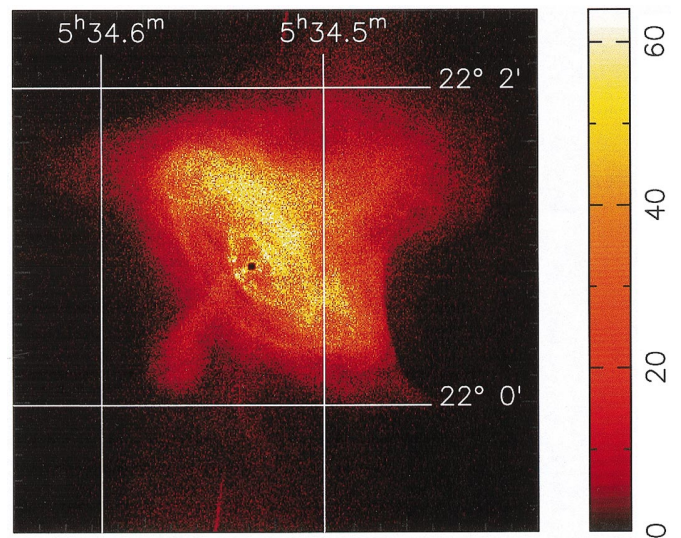
transfer time per row, divided by integration time per frame—and subtracted its spectrum from that of regions labeled B. This results in a 5% decrease in the total rate of regions labeled B, with most of the reduction occurring above 4 keV. We then used this modified spectrum as the "background" in the trailed-image regions labeled T.

3. RESULTS: MORPHOLOGY

Figure 2 shows a $200'' \times 200''$ image of the Crab Nebula, extracted from the S3 full-frame image (Fig. 1). The *Chandra* image clearly shows the X-ray torus (Aschenbach & Brinkmann 1975) and jet and counterjet previously observed (Brinkmann et al. 1985; Hester et al. 1995; Greiveldinger & Aschenbach 1999), which define the southeast-to-northwest axis of the inner Crab Nebula. On somewhat larger scales, the image shows a sharply bounded notch (west-southwest of the pulsar) into the X-ray nebular emission, earlier associated with the "west bay" of the Crab Nebula (Hester et al. 1995). Visible-light polarization maps of the Crab Nebula (Schmidt, Angel, & Beaver 1979; Hickson & van den Bergh 1990) demonstrate that the magnetic field is parallel to the boundary of this notch, thus excluding the X-ray–emitting relativistic electrons from the west bay.

Of course, it is for scales from $1''$ to $10''$ that *Chandra* provides unique information on X-ray structure. To call attention to specific features, we processed the image (Fig. 2) using the flux-conserving adaptive-smoothing algorithm CSMOOTH (Ebeling, White, & Rangarajan 2000) from the *Chandra* Interactive Analysis of Observations (CIAO) package. Figure 3 thus emphasizes small-scale structure, sometimes artificially. To avoid misinterpretation, we use it only in conjunction with the raw image.

The most striking feature of the X-ray image is the inner ring, lying between the pulsar and the torus, which may correspond to a shock in the pulsar wind (Rees & Gunn 1974; Kennel & Coroniti 1984). Comparing the *Hubble* image (Hester et al. 1995) with the *Chandra* image, we find that the positions
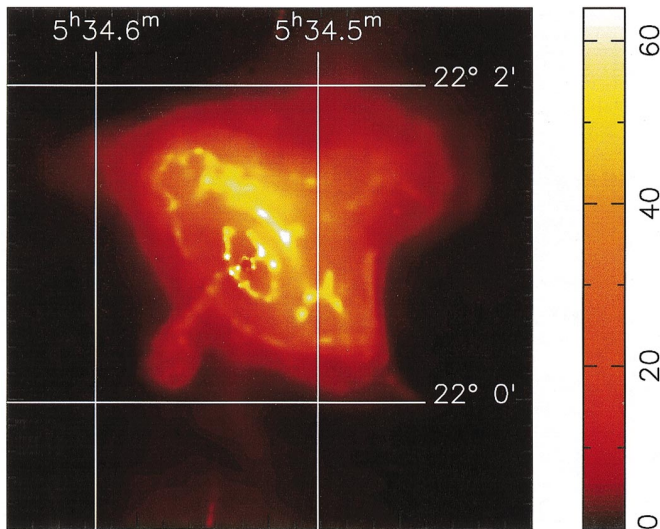
FIG. 3.—Adaptively smoothed *Chandra* HETG–ACIS-S image of the central $200'' \times 200''$ of the Crab Nebula. The processed image accentuates small-scale structure, sometimes artificially, but is useful in identifying specific features in the raw image (Fig. 2). The color bar indicates counts per pixel.
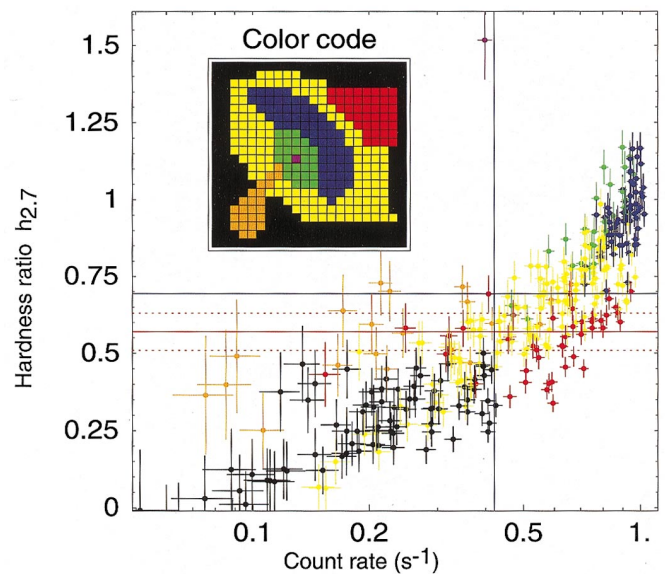

FIG. 4.—Distribution of X-ray hardness in the Crab Nebula. The scatter diagram, color-coded by location in the nebula, shows hardness $h_{2.7}$ (§ 4) against count rate in $5'' \times 5''$ spatial bins. The horizontal red line denotes average hardness (*solid line*) and associated error (*dashed line*) of the trailed image; the horizontal violet line, average hardness of the timed-exposure image, which is biased by pileup effects (§ 2). The outer nebula is softer than the trailed-image average; the jet and counterjet (and its cocoon) have about average hardness. Note that these data are not quantitatively correct at higher count rates, due to pileup effects.

of the visible-light "wisp 1" and the "counterwisp" correspond—at least in projection—approximately to the northwest and southeast quadrants, respectively, of the X-ray inner ring. On the ring, reside a few compact (about $3''$) knots, one lying southeast of the pulsar, along the projected inward extension of the jet. The surface brightness of this knot is too high to be explained as the superposition of the ring's and jet's surface brightnesses.

Having a semimajor axis of about $14''$ (0.14 pc) and a semiminor axis of about $7''$ (0.07 pc), the projected rotational-symmetry axis of the inner ring lies about 58° west of north. The rotational-symmetry axis lies about 30° out of the celestial plane, consistent with tilts estimated for the X-ray torus (Aschenbach & Brinkmann 1975) and for various visible-light structures (Hester et al. 1995).

The most provocative feature of the X-ray torus is the apparent circular structure at each extremity, which resembles the limb-brightened cross-section of a hollow-tube ring torus, with $8''$ (0.08 pc) tube radius. Such structures, if indeed present, significantly constrain models for the inner Crab Nebula. The apparent tube geometry may indicate a role for relativistic ions with Larmor radii on this scale (Gallant & Arons 1994) or a toroidal current which generates a meridional magnetic field wrapping the torus.

Elsewhere, the torus exhibits circumferential fibrous texture but no knots. As noted previously (Aschenbach & Brinkmann 1975), the surface brightness varies significantly with toroidal azimuth, which has been interpreted (Pelling et al. 1987; Greiveldinger & Aschenbach 1999) as resulting from moderate relativistic beaming. In contrast, the surface brightness of the inner ring is more uniform in azimuth (except for the knots), indicating that relativistic beaming is less significant for it than for the torus. Measured from the center of the torus to the center of its tube, the semimajor and semiminor axes are approximately $38''$ (0.37 pc) and $18''$ (0.17 pc), respectively. The rotational-symmetry axis of the toroid lies about 48° west of north and about 28° out of the celestial plane. Because the boundary of the torus is rather diffuse and dependent upon

azimuth, these values are less certain than those for the inner ring. Nevertheless, the in-plane orientation of the torus differs noticeably from that of the inner ring, suggesting that the torus is warped.

The *Chandra* image probes the jet (to the southeast) and counterjet (to the northwest) at higher resolution than previous images with *Einstein* (Brinkmann et al. 1985) or with *ROSAT* (Hester et al. 1995; Greiveldinger & Aschenbach 1999). Although the *Chandra* image shows little additional structure or fibrous texture in the jet or counterjet (or "cocoon" encasing it), it traces them inward closer to the pulsar than previously possible—at least to its projection onto the inner ring. Besides the knot at the projected intersection of the jet with the inner ring, there seems to be another knot, between the inner ring and the pulsar, on the extension of the jet to inside the inner ring. Due to pileup around the image of the pulsar, we cannot exclude that this feature is an artifact. On the other hand, *HST* images (Hester et al. 1995) exhibit similar structure ("knot 2" and "anvil") in this region (a few arseconds southeast of the pulsar). However, we need not expect features in the inner Crab Nebula to be static (e.g., Scargle 1969; Hester et al. 1995; Greiveldinger & Aschenbach 1999). Indeed, those regions that show the brightest X-ray emission tend to correspond to especially dynamic structure (Hester 1998), supporting the interpretation of these features as shocks in the polar jet (Hester et al. 1995).

4. RESULTS: SPECTRAL VARIATIONS

In examining the spectral distribution, we use standard flight grades (*ASCA* grades 02346), for which response matrices currently exist. First, we define the hardness $h_{2.7}$ as the ratio of flux above 2.7 keV to that below 2.7 keV. This energy boundary

fairly well separates events above the iridium-M_V and gold-M_V edges in the instrumental response from those below. We establish from the trailed image (§ 2), which is free of pileup, that $h_{2.7} = 0.57 \pm 0.06$ for the Crab Nebula as a whole. To search for spectral variations within the Crab Nebula, we determine $h_{2.7}$ for each $5'' \times 5''$ bin of a 22×22 array (region Z of Fig. 1).

Figure 4 displays the distribution of hardness $h_{2.7}$ within the Crab Nebula. For count rates below about 0.7 s^{-1}, many $5'' \times 5''$ bins have hardness *less* than the nebular average. This *cannot* result from pileup, which only hardens the spectrum. Obviously, because there are many bins with hardness ratios *below* the average, some of the remaining bins must be *above* average. Thus, the majority of the high count-rate data, although artificially harder due to pileup, is nonetheless truly harder than the average—i.e., there are real variations of X-ray hardness within the Crab Nebula. The outer nebula is significantly softer than the average, as expected for synchrotron losses and previously observed for the visible (Scargle 1969; Veron-Cetty & Woltjer 1993) and ultraviolet (Hennessy et al. 1992) continua. The jet and counterjet (and its cocoon) have hardness comparable to the average, whereas the inner ring appears to be harder. However, the higher contrast structure in the inner ring means that the peak surface brightness in each

bin may significantly exceed the average in the bin, leading to more pileup than suggested by the mean surface brightness. Consequently, although the hardness data indicate a correlation with morphology, the values are not quantitatively accurate.

Unfortunately, the surface brightness of the torus and inner ring is so high that pileup precludes accurate determination of the spectrum of these regions. However, we did analyze the spectral distribution, using XSPEC (Arnaud 1996), of the trailed image and of the timed-exposure image of the outer Crab Nebula. For the trailed image, we fit the spectrum obtained from region T of Figure 1, which is matched to the same range of columns covered by region Z (used in the hardness analysis), but excludes the pulsar.

Current uncertainties in the detector's response below 1 keV and in the zeroth-order effective area result in systematic errors in the spectral analysis. Consequently, we are skeptical of the absolute values of the best-fit spectral parameters. However, because these systematic effects comparably influence the fits for the trailed image and for the outer Crab Nebula, we believe that the relative values are significant. For a column density $N_H = 3.45 \times 10^{21}$ cm^{-2} (Schattenburg & Canizares 1986), we find that the spectral index of the outer Crab Nebula is steeper than that of the average nebula by 0.62; for 2.35×10^{21} cm^{-2} (formal best-fit value), by 0.50.

REFERENCES

Arnaud, K. A. 1996, in ASP Conf. Ser. 101, Astronomical Data Analysis Software and Systems V, ed. G. Jacoby & J. Barnes (San Francisco: ASP), 17
Aschenbach, B., & Brinkmann, W. 1975, A&A, 41, 147
Begelman, M. C., & Li, Z.-Y. 1992, ApJ, 397, 187
Brinkmann, W., Aschenbach, B., & Langmeier, A. 1985, Nature, 313, 662
Coroniti, F. V. 1990, ApJ, 349, 538
Dobrowolny, M., & Ferrari, A. 1976, A&A, 47, 104
Ebeling, H., White, D., & Rangarajan, V. 2000, MNRAS, in press
Emmering, R. T., & Chevalier, R. A. 1987, ApJ, 321, 334
Gallant, Y. A., & Arons, J. 1994, ApJ, 435, 230
Greiveldinger, C., & Aschenbach, B. 1999, ApJ, 510, 305
Hennessy, G. S., et al. 1992, ApJ, 395, L13
Hester, J. J. 1998, in Proc. International Conf. Neutron Stars and Pulsars, Neutron Stars and Pulsars: Thirty Years after the Discovery, ed. N. Shibazaki et al. (Tokyo: Universal Academy Press), 431

Hester, J. J., et al. 1995, ApJ, 448, 240
Hickson, P., & van den Bergh, S. 1990, ApJ, 365, 224
Kennel, C. F., & Coroniti, F. V. 1984, ApJ, 283, 694
Michel, F. C. 1985, ApJ, 288, 138
———. 1994, ApJ, 431, 397
Pelling, R. M., Paciesas, W. S., Peterson, L. E., Makishima, K., Oda, M., Ogawara, Y., & Miyamoto, S. 1987, ApJ, 319, 416
Rees, M. J., & Gunn, J. E. 1974, MNRAS, 167, 1
Scargle, J. D. 1969, ApJ, 156, 401
Schattenburg, M. L., & Canizares, C. R. 1986, ApJ, 301, 759
Schmidt, G. D., Angel, J. R. P., & Beaver, E. A. 1979, ApJ, 227, 106
Veron-Cetty, M. P., & Woltjer, L. 1993, A&A, 270, 370
Weiler, K. W., & Panagia, N. 1978, A&A, 70, 419